ACS SENSORS

pubs.acs.org/acssensors

Article

Facile Synthesis of Co_3O_4/$CoMoO_4$ Heterostructure Nanosheets for Enhanced Acetone Detection

Lu Song, Jaewan Ahn, Liangliang Xu,* Jong Won Baek, Euichul Shin, and Il-Doo Kim*

Cite This: *ACS Sens.* 2022, 7, 3540−3550

Read Online

ACCESS | Metrics & More | Article Recommendations | Supporting Information

ABSTRACT: Although p-type semiconductors exhibit highly selective and stable chemiresistive gas sensing performances compared to conventional n-type semiconductors, their low sensitivity had long impeded their practical development. In this work, we developed highly porous Co_3O_4/$CoMoO_4$ heterostructure nanosheets (NSs) with enhanced sensitivity and superior stability toward acetone gas through a facile solution-based approach with Mo-impregnated Co-based metal−organic frameworks as the starting material. The spontaneous formation of a large number of p−p heterojunctions at the Co_3O_4−$CoMoO_4$ interface would facilitate the adsorption of oxygen and acetone molecules, as verified by density functional theory calculations. Consequently, experimental results showed that the Co_3O_4/$CoMoO_4$ NSs have a greatly enhanced response of 8.5 toward 5 ppm acetone, which is 7.1 times higher than that of pure Co_3O_4 NS, without involving any noble metal catalysts. Moreover, the limit of detection of the Co_3O_4/$CoMoO_4$ NSs was as low as 10 ppb. Altogether, we propose that our synthetic approach for the engineering of p−p heterojunctions is an effective strategy for the future development of highly practical and sensitive gas sensors based on p-type semiconductors.

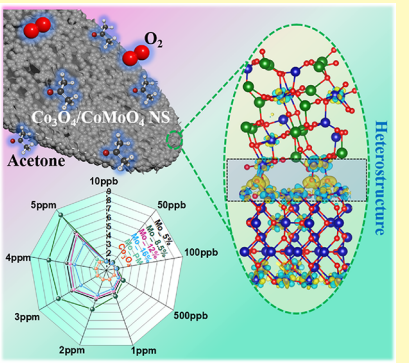

KEYWORDS: *nanosheets, heterojunction, p-type metal oxides, acetone, gas sensors*

Inevitably, the rapid industrialization of emerging economies around the world is contributing to the release of various toxic volatile organic compounds (VOCs) into the atmosphere, which is a major health hazard for the general population. Among the VOCs, acetone is a common byproduct of research and industrial operations,[1] the prolonged exposure to which results in liver and kidney failure in humans.[2] To effectively prevent accidental acetone exposure in the workplace and guarantee the safety and health of workers, therefore, we must develop reliable sensors that can provide accurate, quantitative detection capability toward acetone gases in real-time.[3]

Semiconducting metal oxide (SMO)-based gas sensors have been widely utilized for the detection of various target gas molecules, including VOCs, in a highly sensitive manner. Up to now, various n-type SMOs such as SnO_2,[4] WO_3,[5] In_2O_3,[6] and Fe_2O_3[7] have been widely explored for use as sensing material. Pristine p-type SMOs, on the other hand, have been rarely studied in this application owing to their inherently low response. Specifically, according to a study by Hübner et al.,[8] the response of a p-type SMO-based sensor was about equal to the square root of that of an n-type SMO-based sensor with identical morphologies. Nevertheless, p-type SMOs such as Co_3O_4,[9] NiO,[10] CuO,[11] Cr_2O_3,[12] and Mn_3O_4[13] have recently received a fair share of attention owing to their high catalytic reactivity and relatively low cost as chemiresistive sensing materials.[9] In particular, many p-type SMOs act as catalysts for the selective oxidation of VOCs, which promotes the selective response of the sensor toward the target VOCs.[14] Given these inherent advantages of p-type SMOs toward selective gas sensing, as long as the issues with the low sensitivity of p-type SMOs are resolved through a more in-depth materials design, we should be able to achieve a practically viable sensor system based on p-type SMOs.

One representative type of a p-type SMO is Co_3O_4, a catalytically active material typically used as a photocatalyst[15] or an electrocatalyst,[16] which makes it a suitable candidate for selective gas sensing applications.[9] Specifically, considerable amounts of studies have been conducted to explore and improve the gas-sensing characteristics of Co_3O_4 by modifying their electronic structure. For instance, Li et al.[17] synthesized Co_3O_4 nanocages for selective acetone detection, which was further sensitized with Au to improve the sensing performance. In spite of its effectiveness, noble metal catalysts increase the cost of the sensing material, and the catalyst nanoparticles are prone to aggregation in high-temperature environments. As such, noble-metal-free alternatives are more attractive for practical applications. In this regard, Li et al.[18] demonstrated

Received: September 8, 2022
Accepted: October 20, 2022
Published: November 2, 2022

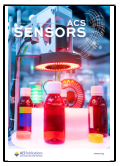

https://doi.org/10.1021/acssensors.2c01969
ACS Sens. 2022, 7, 3540−3550

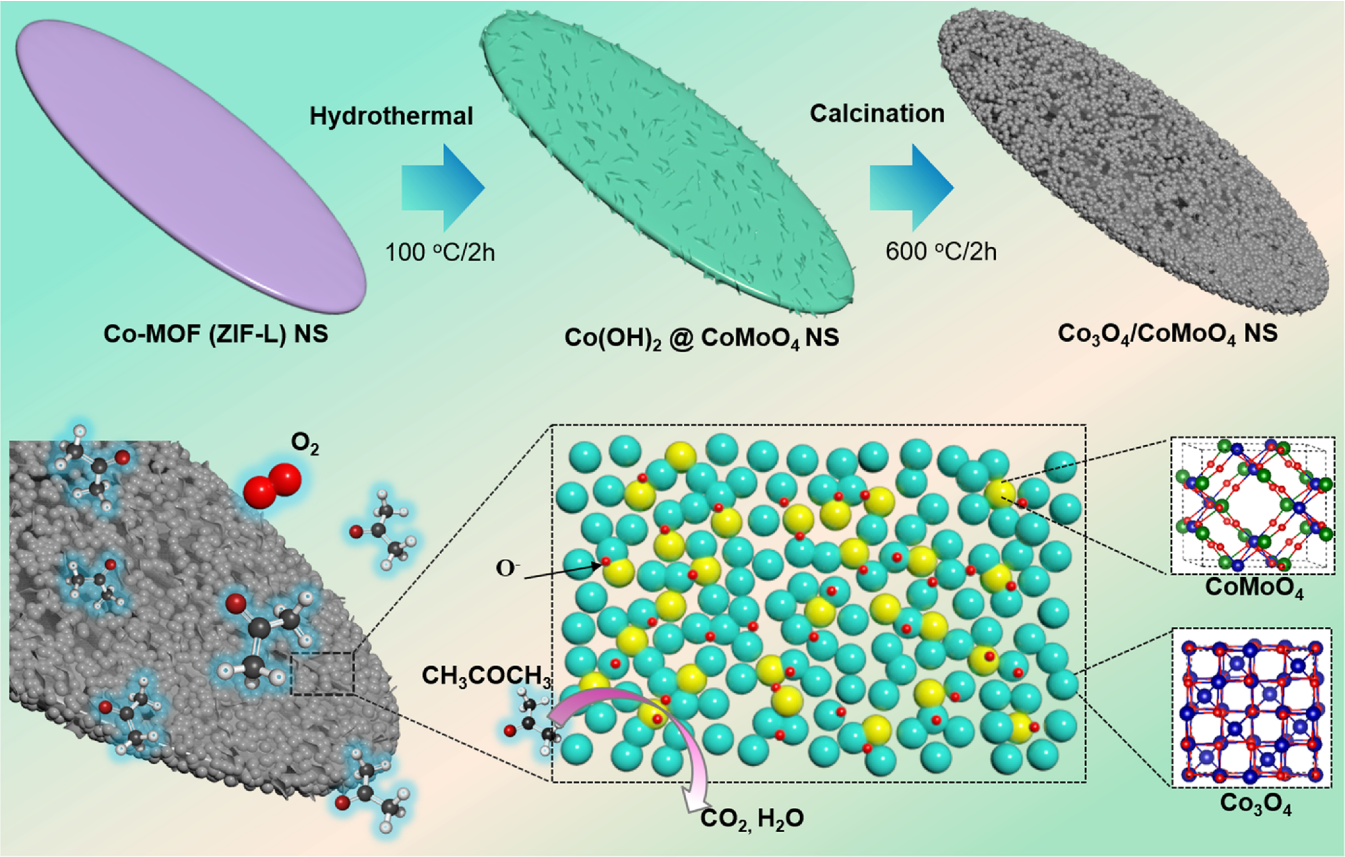

Figure 1. Schematic illustration of the synthesis strategy for the heterojunction $Co_3O_4/CoMoO_4$ NS.

the preparation of flower-like nanostructures consisting of numerous heterojunctions between n-type ZnO phases and p-type Co_3O_4 phases, which can amplify the gas sensing properties through the interface electron flow effect. In n-p junctions, however, the charge carriers readily undergo frequent recombination and mitigate the sensitization, which motivates the exploration of nanostructured SMO-based sensing layers based on abundant p−p heterojunctions.[20] Moreover, two-dimensional materials have been widely used in catalysts such as the hydrogen evolution reaction[19] owing to their highly exposed active sites.[21,22] To this end, while rarely studied in the literature thus far, Co_3O_4-based p−p heterojunction materials should provide an important opportunity for achieving highly sensitive p-type SMO-based chemiresistive sensors.

In this study, metal−organic-framework (MOF) derived p-type Co_3O_4/p-type $CoMoO_4$ (hereafter, $Co_3O_4/CoMoO_4$) heterostructure 2D nanosheets (NSs) were prepared for the first time, and their utility toward acetone detection is demonstrated. Herein, a facile but effective synthesis strategy was introduced by using zeolite imidazole framework-L (ZIF-L) NS as a template. Specifically, ZIF-L acted as the sacrificial host, and the Co^{2+} ions in the porous structure of ZIF-L were converted into $Co(OH)_2$ and $CoMoO_4$ (in the presence of MoO_4^{2-} ions) for their regrowth onto the template upon hydrothermal reaction, the former of which was calcined into Co_3O_4 in the subsequent step to produce heterostructured $Co_3O_4/CoMoO_4$ NSs. The experimental results reveal that the acetone sensing behavior of heterostructured $Co_3O_4/CoMoO_4$ NSs is superior to that of pristine Co_3O_4 and physically mixed (PM)-$Co_3O_4/CoMoO_4$ composite sensors as control samples, in terms of higher sensitivity, ultralow limit of detection (10 ppb), and superior long-term stability. This study paves a new, cost-effective pathway to improve the gas sensing performance of p-type SMO through constructing p−p heterojunction structures.

EXPERIMENTAL SECTION

Materials. Cobalt nitrate hexahydrate ($Co(NO_3)_2{\cdot}6H_2O$), 2-methylimidazole (2-MIM), sodium molybdate dihydrate ($Na_2MoO_4{\cdot}2H_2O$), and ethanol were purchased from Sigma-Aldrich. All chemicals were used as received without further purification.

Synthesis of Co-MOF NS. A total of 8 mmol of 2-MIM and 1 mmol of $Co(NO_3)_2{\cdot}6H_2O$ were dissolved in 20 mL of deionized water. Then, the two solutions were mixed in a beaker, and the resultant solution turned purple immediately. After the reaction at room temperature for 5 h, the sample was collected by using centrifugation, and collected Co-MOF NS was washed in ethanol several times and dried at 60 °C for 5 h.

Synthesis of $Co_3O_4/CoMoO_4$ NS. A total of 0.25 g of Co-MOF NS synthesized above was dispersed in 45 mL of deionized water containing $Na_2MoO_4{\cdot}2H_2O$ (various amounts: 0.01, 0.02, 0.03, and 0.04 g corresponding to $Co_3O_4/CoMoO_4$ (5 at. % Mo), $Co_3O_4/CoMoO_4$ (8.5 at. % Mo), $Co_3O_4/CoMoO_4$ (12 at. % Mo), and $Co_3O_4/CoMoO_4$ (16 at. % Mo), respectively) uniformly by ultrasonication for 5 min to form a suspension (for clarification, the atomic ratios reported in this manuscript corresponds to the actual measured values as confirmed by inductively coupled plasma mass spectrometry (ICP-MS) measurements). The resultant suspension was maintained in an oven at 100 °C for 2 h. Next, the sample was collected using a vacuum filter, and collected $Co(OH)_2$@Mo NS was washed using ethanol and dried at 60 °C for 5 h. At last, the prepared $Co(OH)_2$@$CoMo_4$ NS was first calcined at 350 °C for 2 h with a

https://doi.org/10.1021/acssensors.2c01969
ACS Sens. 2022, 7, 3540−3550

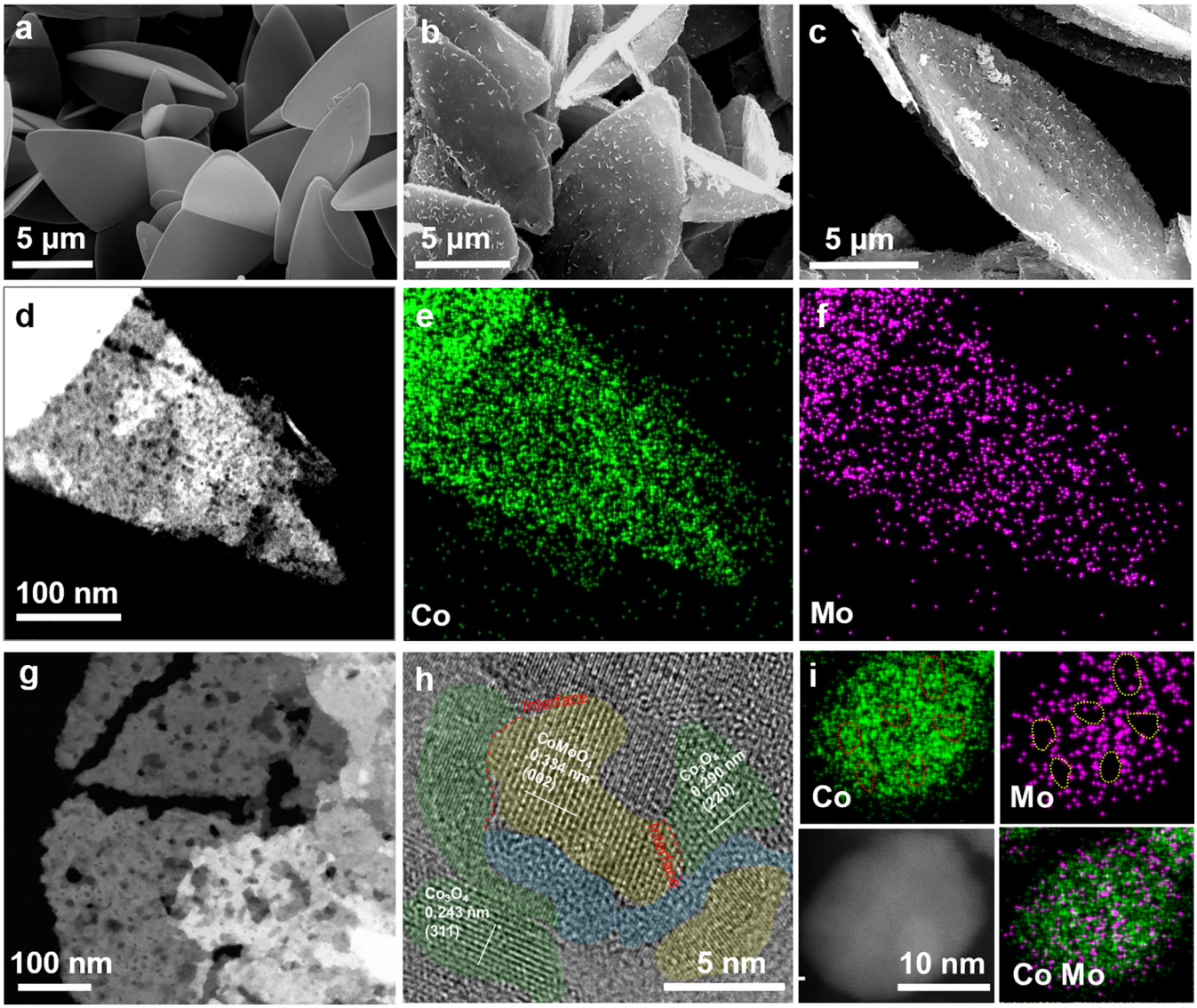

Figure 2. SEM images of (a) Co-MOF NS, (b) $Co(OH)_2$@Mo NS, and (c) $Co_3O_4/CoMoO_4$ NS. (d, g) STEM, (h) HRTEM images, and (e, f) low-resolution and (i) high-resolution EDS mapping of $Co_3O_4/CoMoO_4$ NS.

ramping rate of 5 °C/min, followed by calcination at 600 °C/min for 2 h with a ramping rate of 10 °C/min.

Synthesis of Co_3O_4 NS, $CoMoO_4$, and Physically Mixed (PM)-$Co_3O_4/CoMoO_4$. The synthesis of Co_3O_4 NS is similar to that of $Co_3O_4/CoMoO_4$ NS except for the absence of the reaction with an aqueous solution of $Na_2MoO_4{\cdot}2H_2O$. $CoMoO_4$ is prepared as follows: 7.0 mmol $CoCl_2{\cdot}6H_2O$, 1.0 mmol $(NH_4)_6\ Mo_7O_{24}{\cdot}4H_2O$, and 28 mmol $CO(NH_2)_2$ are dissolved in 70 mL of deionized water homogenously. Next, the solution is transferred into a 100 mL Teflon-lined autoclave followed by a heat treatment at 120 °C for 10 h. Then, the sample with pink color is collected following the $Co_3O_4/CoMoO_4$ NS collecting method. Physically mixed $Co_3O_4/CoMoO_4$ (denoted as PM-$Co_3O_4/CoMoO_4$) is prepared by sonicating 1 mL of ethanol solution containing 197 mg of Co_3O_4 and 19.6 mg of $CoMoO_4$ for 15 min (calculated atomic ratio of Mo: 8.5%).

Preparation of Sensors and Evaluation of Gas Sensing Performance. The fabrication of sensors is reported by our previous study.[23] Air and varying concentrations of target gas were injected into the gas-sensing chamber based on 10 min air and 10 min target gas as a complete cycle. The response of sensors was calculated as R_{gas}/R_{air}, where R_{gas} and R_{air} are the resistances in target gas and ambient condition, respectively.

DFT Calculations. The spin-polarized DFT + U (U = 2.0 eV for Co[24]) calculations were performed using the plane-wave projector augmented-wave (PAW) method,[25] applying the semi-local Perdew–Burke–Ernzerhof (PBE) exchange-correlation functional, as implemented in the Vienna ab initio simulation package (VASP) code.[26] More details are given in the Supporting Information.

RESULTS AND DISCUSSION

The synthesis of $Co_3O_4/CoMoO_4$ NSs is illustrated in Figure 1. In the first step, the Co-MOF nanosheet was homogeneously grown in an aqueous growth solution containing Co precursors ($Co(NO_3)_2{\cdot}6H_2O$) and the organic linker molecules (2-methylimidazole). The as-obtained Co-MOF sheets were subsequently mixed with Na_2MoO_4 in an aqueous solution and then subjected to a hydrothermal treatment (schematically illustrated in Figure S1). In this case, the Co-MOF is a porous structure with a large surface area and Co^{2+} is evenly distributed in the porous structure of Co-MOF.[27] Meanwhile, Na_2MoO_4 plays two roles: generating molybdate acid radicals (MoO_4^{2-}) and inducing an alkaline environment (OH^-). Thus, the Co^{2+} ions reacted with either MoO_4^{2-} or

https://doi.org/10.1021/acssensors.2c01969
ACS Sens. 2022, 7, 3540−3550

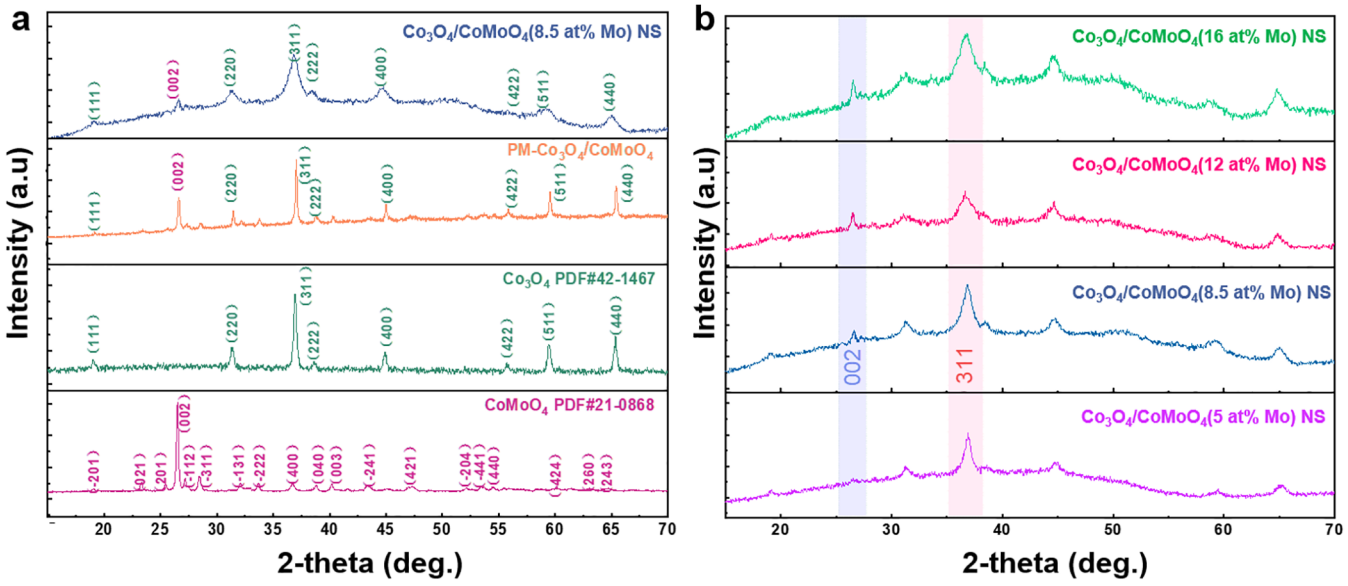

Figure 3. XRD patterns of (a) Co_3O_4 NSs, $CoMoO_4$, $Co_3O_4/CoMoO_4$ (8.5 at. % Mo) NSs, PM-$Co_3O_4/CoMoO_4$, and (b) $Co_3O_4/CoMoO_4$ (5–16 at. % Mo) NSs.

OH^- ions in the aqueous solution to form $CoMoO_4$ and $Co(OH)_2$, respectively, which is readily deposited onto the template. The regrowth process continues, transforming the MOF into a $Co(OH)_2/CoMoO_4$ heterostructure while maintaining the initial 2D sheet-like morphology of the ZIF-L template. The $Co(OH)_2$ portion of this heterostructure could be further oxidized to Co_3O_4 through calcination, ultimately yielding the heterostructured $Co_3O_4/CoMoO_4$ NSs.

Scanning electron microscopy (SEM) and transmission electron microscopy (TEM) analyses were carried out to investigate the morphologies and structures of the as-made samples. The SEM images in Figure 2a (Figure S2, low magnification SEM image) show that the Co-MOF NSs with a smooth surface was successfully obtained through the aqueous reaction. After the hydrothermal process, the NSs could maintain their 2D morphology but turned slightly rough with several debris on the surface (Figure 2b and Figure S3) formed by the *in situ* regrowth and sedimentation of $Co(OH)_2$ and $CoMoO_4$, which are insoluble in water. The NSs retained their structure even after calcination, as shown in Figure 2c and Figure S4. Moreover, TEM images also support the successful synthesis of the NSs as shown in Figure 2d and Figure S5. Notably, the high-resolution scanning TEM (STEM) images in Figure 2g and Figure S6b,c revealed the porous structure of $Co_3O_4/CoMoO_4$ NSs, wherein the abundant pores on NSs (Figure S6a) would promote the permeation of gas molecules into the sensing layer for effectively eliciting chemiresistive response. In addition, a homogeneous distribution of Mo on the Co_3O_4-based NS without obvious aggregation is confirmed according to the energy dispersive spectroscopy (EDS) element mapping results (Figure 2e,f). We further conducted a high-magnification EDS mapping as shown in Figure 2i; the area with concentrated Co signals and empty Mo signals (encircled in yellow dotted lines) is ascribed to the crystalline Co_3O_4, while the remaining area showing both Co and Mo signals is assumed to be $CoMoO_4$. Furthermore, the HRTEM image in Figure 2h presents the lattice fringes with interplanar parameters of 0.290, 0.243, and 0.334 nm, corresponding to the (220) and (311) planes of cubic Co_3O_4 and the (002) plane of monoclinic $CoMoO_4$, respectively. Altogether, we could confirm that nanoscale grains of Co_3O_4 and $CoMoO_4$ coexist in an even mixing, together constituting the porous 2D NS structure and that this structure would facilitate highly sensitive gas sensing performances.

To investigate the crystal structure of the as-synthesized NSs, we performed powder X-ray diffraction (XRD) analyses on the $Co(OH)_2$@Mo NS, $Co_3O_4/CoMoO_4$ NSs (8.5 at. % Mo, real value as confirmed by ICP-MS measurements), PM-$Co_3O_4/CoMoO_4$, Co_3O_4 NSs, and $CoMoO_4$ (Figure 3a, and Figure S8). For reference, the XRD patterns of Co_3O_4 NSs and $CoMoO_4$ each showed peaks assigned to cubic Co_3O_4 (JCPDS, PDF#42-1467) and monoclinic $CoMoO_4$ (JCPDS, PDF#21-0868), respectively. Importantly, the diffraction peaks of $Co_3O_4/CoMoO_4$ NSs as well as the PM-$Co_3O_4/CoMoO_4$ indicated the coexistence of Co_3O_4 and $CoMoO_4$ crystals. As elucidated previously, PM-$Co_3O_4/CoMoO_4$ NS was prepared by physically mixing crystals of Co_3O_4 and $CoMoO_4$, thus exhibiting stronger and sharper diffraction peaks, which indicate low dispersity and better crystallinity. On the contrary, $Co_3O_4/CoMoO_4$ (8.5%) NSs exhibit broadening in their diffraction peaks compared with the other three samples (Figure 3), indicating decreased grain sizes (TEM image in Figure S7a,b) as a result of the *in situ* growth strategy. The minor diffraction peaks (i.e., $(\bar{2}04)$, $(\bar{4}41)$, and (440)) corresponding to $CoMoO_4$ were not strong enough to be observed with clarity. In Figure 3b, as the Mo content increased from 5.0 to 16 at. %, the diffraction peak located at $2\theta = 36.9°$ corresponding to the (311) plane of Co_3O_4 showed a noticeable broadening, which indicates that the growth of Co_3O_4 grains were impeded. Since the main peak located at $2\theta = 26.5°$ corresponding to the (002) plane of $CoMoO_4$ was also becoming stronger, which was attributed to the increasing amount of crystalized $CoMoO_4$, we may conclude that the presence of $CoMoO_4$ prohibited the growth of Co_3O_4 grains. Altogether, the TEM and XRD analyses confirmed that $Co_3O_4/CoMoO_4$ NSs having nanograins with regulated sizes could be successfully prepared through our *in situ* growth strategy, which would induce the formation of a large number

https://doi.org/10.1021/acssensors.2c01969
ACS Sens. 2022, 7, 3540−3550

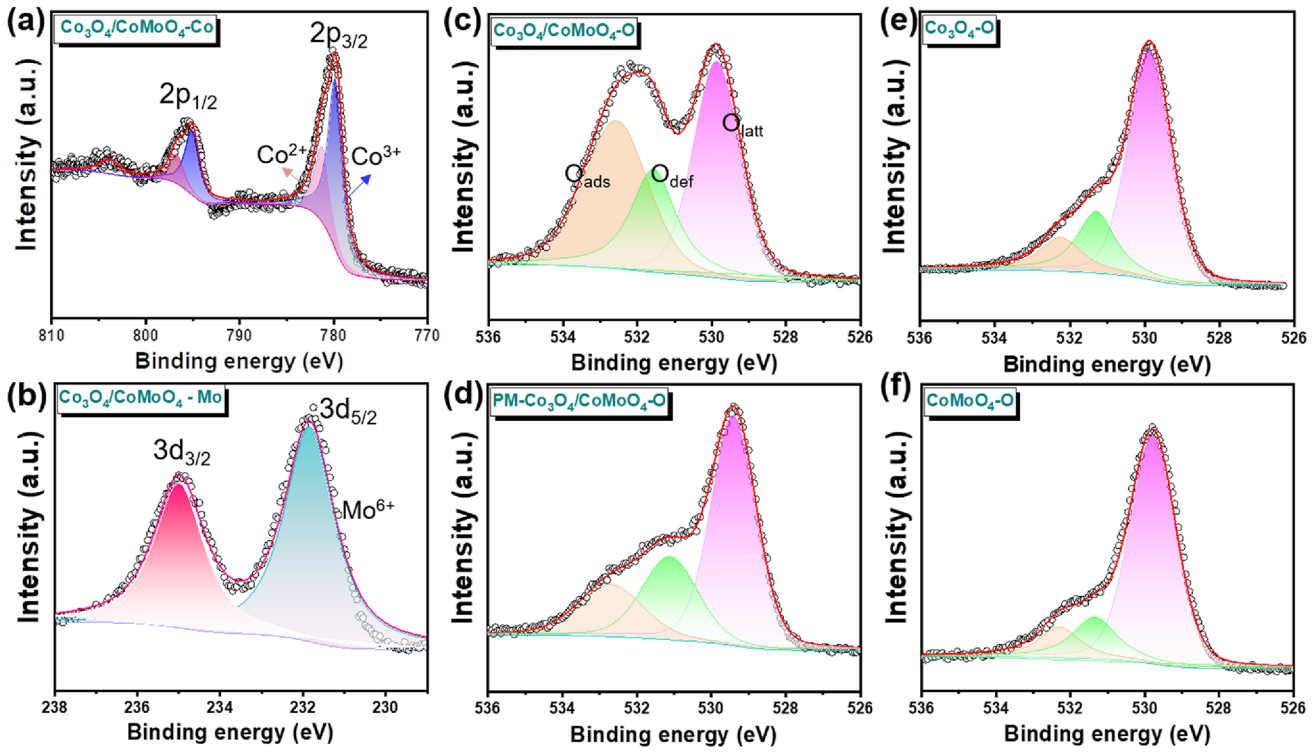

Figure 4. High-resolution XPS scan profile spectra of the (a) Co 2p, (b) Mo 3d region, and (c) O 1s region in $Co_3O_4/CoMoO_4$ (8.5 at. % Mo) NSs. High-resolution spectra in the O 1s region of (d) PM-$Co_3O_4/CoMoO_4$ NS, (e) pristine Co_3O_4 NS, and (f) pristine $CoMoO_4$.

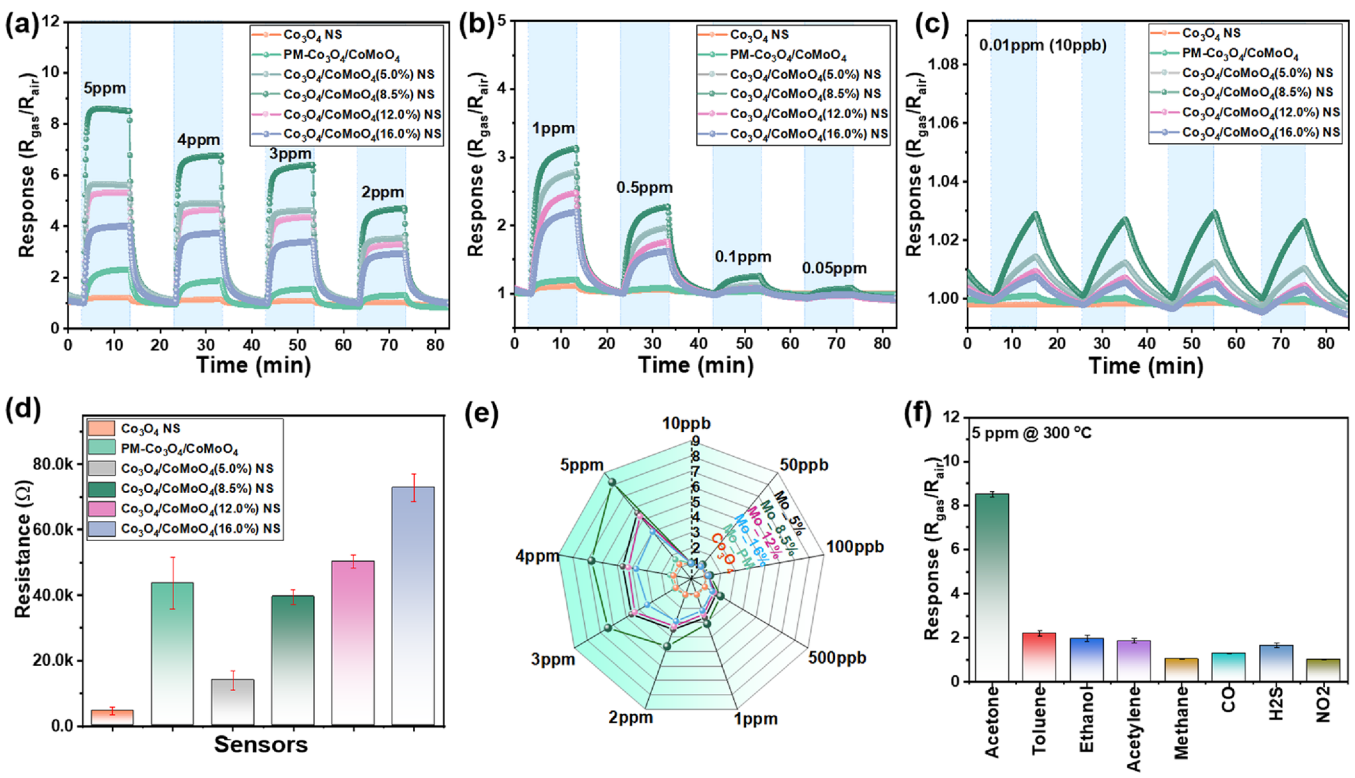

Figure 5. (a–c) Dynamic response and (d–e) plot of the response of Co_3O_4, $Co_3O_4/CoMoO_4$ (5–16 at. % Mo) NSs, PM-$Co_3O_4/CoMoO_4$ toward 5–0.01 ppm acetone gas at 300 °C. (f) Selectivity of $Co_3O_4/CoMoO_4$ (8.5 at. % Mo) NSs to various gases (5 ppm) at 300 °C.

of p-p heterojunctions for improving the sensing performances of p-type Co-based SMOs.

To further analyze the composition and chemical states of the synthesized NSs, X-ray photoelectron spectroscopy (XPS) analyses were performed (Figure 4 and Figure S9–10). The XPS spectra of the as-synthesized $Co_3O_4/CoMoO_4$ NSs revealed the existence of Co 2p, Mo 3d, and O 1s peaks, which confirms the mixed oxide composition. In more detail,

https://doi.org/10.1021/acssensors.2c01969
ACS Sens. 2022, 7, 3540–3550

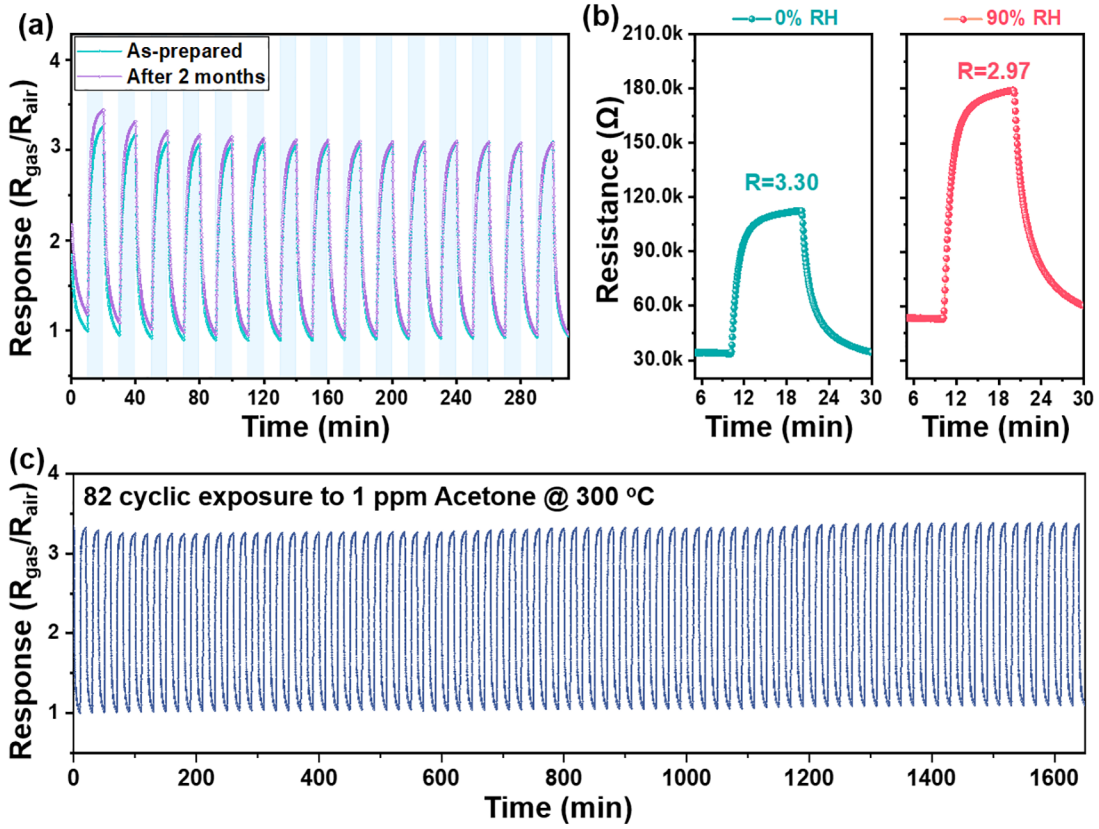

Figure 6. (a) Long-term stability, (b) dynamic resistance transient in dry air and humid air (90% RH), and (c) reliability of heterojunction Co_3O_4/$CoMoO_4$ (8.5 at. % Mo) NSs toward 1 ppm of acetone gas at 300 °C.

the Co 2p region (Figure 4a) showed two main peaks attributed to $2p_{3/2}$ (779.75 eV) and $2p_{1/2}$ (795.01 eV) peaks of Co^{3+}, respectively. Two smaller peaks for the $2p_{3/2}$ (781.26 eV) and $2p_{1/2}$ (796.69 eV) peaks of Co^{2+} were also located. These peaks confirm the coexistence of Co^{3+} and Co^{2+} in the as-prepared NSs, supporting the formation of spinel-structure Co_3O_4. In addition, the two peaks in the Mo 3d region as shown in Figure 4b at 235.0 and 231.9 eV can be assigned to the $3d_{3/2}$ and $3d_{5/2}$ peaks of Mo^{6+} as their peak separation (3.1 eV), respectively, coinciding with that of previously reported values for Mo^{6+}.[28] Furthermore, the spectrum of O 1s can be deconvoluted into three Gaussian peaks at 529.9 (lattice oxygen, denoted as O_{latt}), 531.4 (defect oxygen, denoted as O_{def}), and 532.7 eV (adsorbed oxygen, denoted as O_{ads}). Specifically, the proportion of the combined sum of O_{def} and O_{ads} over the entire O 1s signal (S_{che}) represented the surface chemisorbed oxygen species that can participate in the redox reaction with incoming acetone molecules, inducing a change in resistance.[29−31] The S_{che} in the case of heterostructure Co_3O_4/$CoMoO_4$ (8.5 at. % Mo) NSs (59.9%) was significantly higher than that of pristine Co_3O_4 (32.5%) and $CoMoO_4$ (27.1%), indicating that the heterostructure provides additional chemisorbed oxygen species on the surface. Based on the fact that the S_{che} of PM-Co_3O_4/$CoMoO_4$ was calculated as 43.4%, we concluded that the synergistic effect of the heterojunctions facilitates the chemisorption of oxygen.[32]

To directly evaluate the effect of p-p heterojunctions on improving the gas sensing characteristics of the p-type Co-based SMOs, we characterized the chemiresistive responses of Co_3O_4 NSs, PM-Co_3O_4/$CoMoO_4$, and Co_3O_4/$CoMoO_4$ NSs (with different amounts of $CoMoO_4$) upon exposure to varying concentrations of acetone as well as other interfering gases (C_7H_8, C_2H_5OH, C_2H_2, CH_4, CO, H_2S, NO_2) (Figure 5, more information of sensors are shown in Figure S11). Previous studies on SMO-based gas sensors indicated that the working temperature is a critical parameter that affects the sensing performance since the surface adsorption behavior can directly be affected.[33] Hence, we first optimized the working temperature by exposing Co_3O_4/$CoMoO_4$ NSs, as the representative sample, to acetone of 5 ppm at various working temperatures (200−400 °C). As shown in Figure S12, the Co_3O_4/$CoMoO_4$ NSs exhibited the highest response to 5 ppm acetone at 300 °C; henceforth, the evaluation of the dynamic sensing behavior (to 10 ppb−5 ppm acetone gas) was conducted at 300 °C to establish a fair comparison between each sample.

We then compared the baseline resistance of each sensor as shown in Figure 5d and found that the baseline resistance of Co_3O_4/$CoMoO_4$ (8.5 at. % Mo) NSs (39 kΩ) is much higher than that of Co_3O_4 (4.6 kΩ), which is ascribed to several factors including the inherent poor conductivity of $CoMoO_4$, numerous heterointerfaces that serve as charge barriers, abundant chemisorbed oxygen species,[34] and the grain size effect.[35] We found that the electrical resistances of Co_3O_4/$CoMoO_4$ NSs showed a strong correlation with increased amounts of $CoMoO_4$, supporting our understanding. As shown in Figure 5a, the response of Co_3O_4/$CoMoO_4$ (8.5 at. % Mo) NSs to 5 ppm acetone is shown to be 8.5, which is 7.1 times higher than that of Co_3O_4 NSs (response = 1.2). Similarly, we found that all of the sensors containing both Co_3O_4 and $CoMoO_4$, including the case of the physically mixed sample, can achieve a higher response to acetone gas compared to

https://doi.org/10.1021/acssensors.2c01969
ACS Sens. 2022, 7, 3540−3550

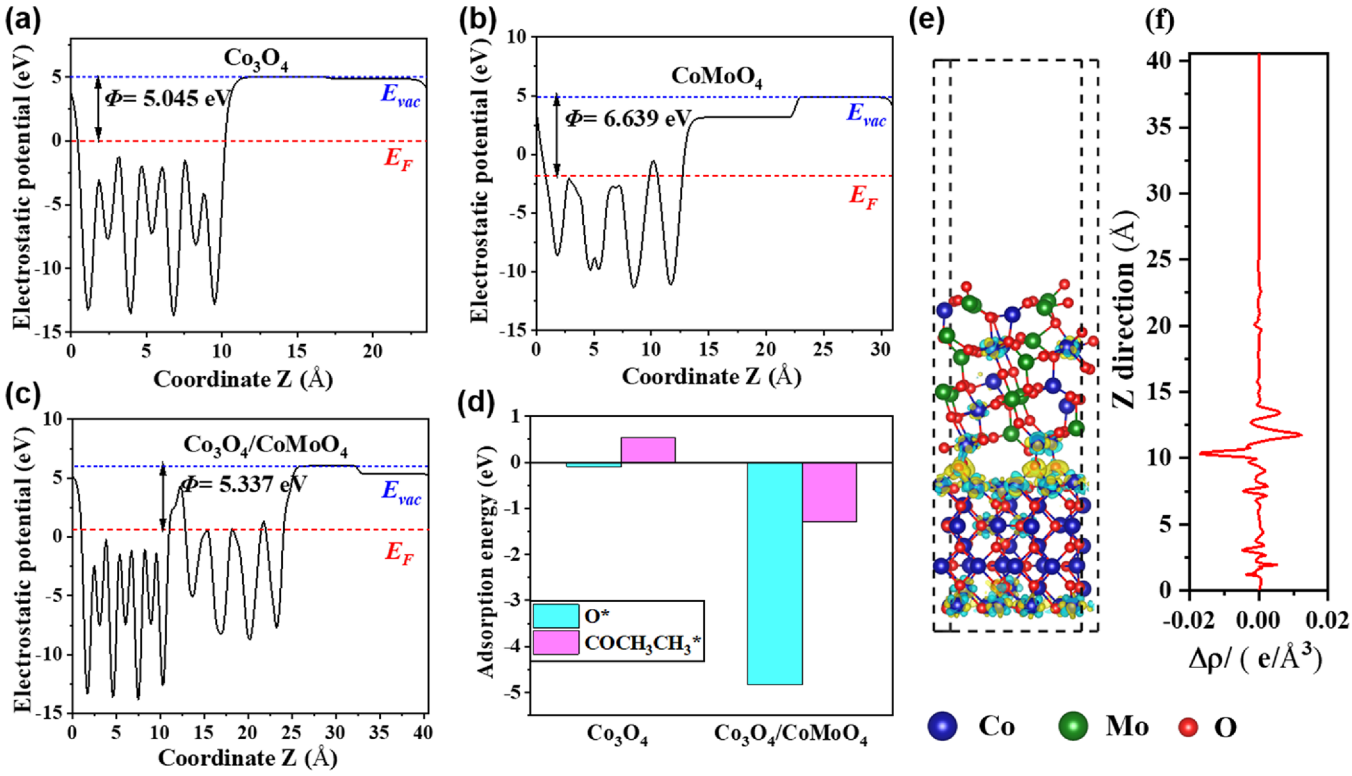

Figure 7. Work functions of (a) Co_3O_4, (b) $CoMoO_4$, and (c) $Co_3O_4/CoMoO_4$ NSs. (The blue and red dashed lines represent the vacuum level and Fermi level.) (d) Adsorption energy of O and acetoen ($COCH_3CH_3$) by Co_3O_4 and $Co_3O_4/CoMoO_4$. (e) $Co_3O_4/CoMoO_4$ 3D charge density difference, and (f) planner average charge density difference.

pristine Co_3O_4, albeit with high baseline resistance. Specifically, the responses of PM-$Co_3O_4/CoMoO_4$ NSs were 2.3, the decreasing response of which is attributed to the limited amount of heterojunction interfaces for physically mixed samples due to the low dispersity of Mo-containing regions (Figure S13).

The dynamic response of the various sensing materials to 50 ppb acetone is shown in Figure S14, from which we found that all of the $CoMoO_4$-containing materials (including the physically mixed sample) exhibited an improved response, while pristine Co_3O_4 NSs showed practically undiscernible changes in the resistance. It is noteworthy that $Co_3O_4/CoMoO_4$ NSs (with different contents of $CoMoO_4$) exhibited an exceptionally low limit of detection (LOD, defined as the lowest concentration of the analyte gas that can be detected) of 10 ppb (Figure 5c). We further investigated their selectivity toward acetone gas by exposing $Co_3O_4/CoMoO_4$ (8.5 at. % Mo) NSs, the representative sample, to various common interfering gases (C_7H_8, C_2H_5OH, C_2H_2, CH_4, CO, H_2S, NO_2), each at a concentration of 5 ppm (Figure 5f, Figure S15). We found that the heterostructured NSs exhibited excellent selectivity toward acetone gas with a significantly higher response (R_{gas}/R_{air} > 8) compared to those of other analytes (R_{gas}/R_{air} < 2.1 for toluene, which was the second-highest). Taken together, we demonstrated that the interface engineered p-type MOSs, such as Co_3O_4, by incorporating numerous heterojunctions in the nanostructure, can effectively enhance the sensing performance.

In real-life applications, the detrimental effects of humidity on the response of the SMO-based gas sensors are often cited as a major development challenge.[36] Since the electrons donated from the water vapor would recombine with electronic holes to decrease the number of charge carriers, the baseline resistance of wet p-type SMOs would increase, as demonstrated in Figure 6b and Figure S16.[37,38] Interestingly, the response of $Co_3O_4/CoMoO_4$ (8.5 at. % Mo) NSs under a high RH of 90% (2.97 toward 1 ppm acetone) was only slightly degraded (9.0%) compared to the response in a dry atmosphere (3.30 toward 1 ppm acetone), demonstrating the resilience of NSs even in a highly humid environment. Furthermore, long-term stability and reliability are also crucial to the practical use of gas sensors. To investigate the acetone sensing stability, the $Co_3O_4/CoMoO_4$ (8.5 at. % Mo) NSs were exposed to 1 ppm acetone for 15 successive cycles, where each cycle consists of a 10 min injection of air (baseline) followed by acetone (target gas). The dynamic response to 1 ppm acetone gas is plotted as shown in Figure 6a, demonstrating stable responses of 3.4 on average (standard derivation of 0.05) throughout 15 cycles with no noticeable fluctuation and/or degradation in the signals. Even after the sensor was kept in ambient conditions for 2 months after initial fabrication, the dynamic response curves of the aged sensors (Figure 6a) were not too different from the as-synthesized sensors, implying the excellent long-term stability of the $Co_3O_4/CoMoO_4$ heterojunction NSs. We further established the reliability of $Co_3O_4/CoMoO_4$ (8.5 at. % Mo) NSs by evaluating it over an extended cyclic exposure of 82 cycles, as illustrated in Figure 6c. Moreover, the stability test results of pristine Co_3O_4 NS and PM-$Co_3O_4/CoMoO_4$ are presented in Figure S17. Altogether, the $Co_3O_4/CoMoO_4$ NSs synthesized in this study can improve the sensing response without further degradation of stability.

To elaborate on the explicit mechanistic details of the chemiresistive sensing of $Co_3O_4/CoMoO_4$ NSs, we performed

https://doi.org/10.1021/acssensors.2c01969
ACS Sens. 2022, 7, 3540−3550

Table 1. Publications on SMO-Based Sensors for Detecting Acetone[a]

sensing materials	$D_{(response)}$	response	LOD	operating temp	ref
PdO−Co_3O_4	R_{gas}/R_{air}	2.51 at 5 ppm	100 ppb	350 °C	36
SnO_2−Co_3O_4	R_{air}/R_{gas}	1.50 at 1 ppm	500 ppb	220 °C	43
IGO@ZnO	R_{air}/R_{gas}	2.10 at 1 ppm	200 ppb	300 °C	44
ZnO−MoS_2	R_{air}/R_{gas}	4.67 at 20 ppm	100 ppb	100 °C with UV	45
Pt−SnO_2	R_{air}/R_{gas}	1.50 at 200 ppb	200 ppb	400 °C	46
Pt−Co_3O_4	R_{gas}/R_{air}	3.50 at 1 ppm	100 ppb	200 °C	47
NiO−Zn_2SnO_4	R_{air}/R_{gas}	5.2 at 5 ppm	100 ppb	300 °C	2
Pt−SnO_2 NTs	R_{air}/R_{gas}	192 at 5 ppm	10 ppb	350 °C	48
Ni_1Sn_3	R_{air}/R_{gas}	6 at 5 ppm	10 ppb	300 °C	49
In_2O_3−AuPt	R_{air}/R_{gas}	3 at 20 ppm	500 ppb	240 °C	50
Pt-loaded Fe_2O_3	R_{air}/R_{gas}	1.10 at 1 ppm	200 ppb	139 °C	51
ZnO:Pt nanostructures	R_{air}/R_{gas}	20.6 at 100 ppm	nr	450 °C	52
Co_3O_4/$CoMoO_4$(8.5 at. % Mo) NSs	R_{gas}/R_{air}	8.50 at 5 ppm1.03 at 10 ppb	10 ppb	300 °C	this work

[a]$D_{(response)}$ is the definition of response, nr = not reported.

additional analyses accompanied by theoretical calculations and considerations. The origin of the chemiresistive response of typical p-type SMO-based sensing materials is the reaction of target gas molecules with chemisorbed oxygen on the sensing layers, which changes the charge carrier population on the surface to modulate the overall resistance.[36,38,39] Specifically, the sensing process involves (i) the chemisorption of oxygen species on the sensing layers (eq 1) resulting in the formation of hole accumulation layers, which helps decrease the resistance of sensors; and the (ii) release of electrons back to the sensing layer and their recombination with holes upon the reaction of acetone molecules with chemisorbed oxygen (eqs 2 and 3), thus increasing the electrical resistance. To identify the energy level between the Co_3O_4 and $CoMoO_4$, ultraviolet photoelectron spectroscopy (UPS) measurements were carried out as shown in Figure S18. The work function (W_f) of Co_3O_4 was calculated as 5.17 eV (5.045 eV from density functional theory (DFT) calculations), while that of the pristine $CoMoO_4$ could not be collected owing to its poor conductivity. According to the calculated W_f of Co_3O_4/$CoMoO_4$ (8.5 at. % Mo) NSs of 5.50 eV, it was speculated that $CoMoO_4$ would exhibit a larger W_f than Co_3O_4, which is also supported by DFT calculations.[40] It seems reasonable to deduce from these results that the formation of the heterojunction interfaces between Co_3O_4 and $CoMoO_4$ domains caused the migration of electrons from Co_3O_4 to $CoMoO_4$, inducing the formation of the depletion layers at the Co_3O_4/$CoMoO_4$ interface. When the surface is exposed to acetone, more electrons will be released back to the sensing layers after the acetone reacts with chemisorbed oxygen species to amplify the change in resistance.

$$O_2(g) \rightarrow 2\,O^-_{(ads)} + 2\,h^+ \quad (1)$$

$$CH_3COCH_3(g) + O^-_{(ads)} \rightarrow CH_3COC^+H_2 + OH^- + e^- \quad (2)$$

$$CH_3COCH_3(g) + 2\,O^-_{(ads)} \rightarrow CH_3O^- + C^+H_3 + CO_2 + 2\,e^- \quad (3)$$

Furthermore, we carried out systematic DFT calculations to support the UPS measurement data, ultimately to unravel the enhancement mechanisms of the p-p heterojunction toward acetone sensing. As shown in Figure 7, the work functions of Co_3O_4 and $CoMoO_4$ were found to be 5.045 and 6.639 eV, respectively. When the Co_3O_4/$CoMoO_4$ heterojunction is formed, the Fermi level is equalized across the interface as the charge carriers are transported across the junction, indicated by the measured work function of 5.337 eV as shown in Figure 7c. Subsequently, as shown in Figure 7d, we calculated the adsorption energy of the O atom and $COCH_3CH_3$ on the model surfaces of Co_3O_4 (E_{O^*} = −0.09 eV, $E_{COCH3CH3^*}$ = +0.53 eV) and Co_3O_4/$CoMoO_4$ (E_{O^*} = −4.83 eV, $E_{COCH3CH3^*}$ = −1.29 eV), showing that the heterojunction facilitates a more favorable chemisorption of either species. This is corroborated by our experimental observations that the heterojunction exhibits a larger amount of chemisorbed oxygen and provides a significant increase in sensitivity for acetone gas detection. Specifically, Figure 7e shows a local increase in the electron density at the Co_3O_4/$CoMoO_4$ interface, assisting the formation of a stable chemical bond. The yellow electron cloud represents the received electrons, and the cyan electron cloud indicates the lost electrons. Figure 7f shows a violent oscillation of the average planar charge density plot at the interface, which supports the active electron exchange at the interface. From Bader charge calculations (Table S1), we could ascertain that this charge transfer occurs across the Co_3O_4/$CoMoO_4$ heterojunction, with 2.6 e of charge transferred from Co_3O_4 to $CoMoO_4$.

Overall, the experimental data and DFT calculations together illustrate a clear mechanistic picture. Numerous p-p heterojunctions formed at Co_3O_4/$CoMoO_4$ interfaces would cause the electron transfer owing to different work functions until the Fermi levels are equal; thus, the hole accumulation layer and electron depletion layer formed on the lower work function side and higher work function side, respectively. A higher amount of chemisorbed oxygen species could be found owing to the enlarged electron accumulation layer.[41] The unique electronic structure between the heterostructure interfaces has been also demonstrated in hydrogen evolution catalysts.[42] The subsequent chemical reaction between acetone gas molecules and chemisorbed oxygen leads to more electrons being released and recombining with holes, generating chemiresistive responses and contributing to the enhanced sensitivity to acetone gas. We note that, even when compared to state-of-the-art sensors including those based on n-type SMOs or those sensitized with noble metal catalysts, the Co_3O_4/$CoMoO_4$ NSs having numerous p-p heterojunctions exhibited superior sensing response and a record-low LOD of 10 ppb (Table 1).

https://doi.org/10.1021/acssensors.2c01969
ACS Sens. 2022, 7, 3540−3550

CONCLUSIONS

In this work, we have synthesized the $Co_3O_4/CoMoO_4$ heterojunction NSs through the MOF-derived *in situ* growth method as a p-type sensing layer not only with high selectivity but also improved sensitivity and outstanding stability toward the detection of acetone gas. Through our demonstration, we highlight the practical relevance and effectiveness of the engineered p-p heterojunctions formed at the interfaces of $Co_3O_4/CoMoO_4$ NSs. The p-p heterojunction favors the chemisorption of both chemisorbed oxygen species and acetone target gas, inducing a significant enhancement in the response to 5 ppm acetone gas from 1.2 for pristine Co_3O_4 to 8.5. Moreover, even when repeatedly exposed to 1 ppm acetone for over 15 cycles at 300 °C, the $Co_3O_4/CoMoO_4$ NSs remained stable with an average response of 3.4 with no noticeable decay in the response. Most notably, the synthesized $Co_3O_4/CoMoO_4$ NSs were effective in detecting ultralow concentrations of acetone with a limit of detection (LOD) of 10 ppb. Together with DFT calculations to adequately describe our experimental observations, we could elucidate the particular roles played by the p-p heterojunction in enhancing the sensing response. Moving forward, our facile approach to engineer p-p heterojunctions for improving the reliability of p-type SMO-based chemiresistive sensors not only provides an immediately useful solution for acetone sensing but also expands our insights for establishing the rational design of practical p-type SMO-based sensors with high selectivity as well as sensitivity.

ASSOCIATED CONTENT

Supporting Information

The Supporting Information is available free of charge at https://pubs.acs.org/doi/10.1021/acssensors.2c01969.

Detailed experimental information, SEM images of synthesized NSs, STEM image of $Co_3O_4/CoMoO_4$ NSs, XRD of mid product, XPS of Co_3O_4 and PM-$Co_3O_4/CoMoO_4$ NSs, EDS mapping of $Co_3O_4/CoMoO_4$ NSs, dynamic response of different samples toward 50 ppb acetone at 300 °C, response of sensors at different humidities, selectivity of sensors at various working temperatures, dynamic stability of Co_3O_4 NS and PM-$Co_3O_4/CoMoO_4$ NSs, UPS analysis results, and the raw data of Bader charge transfer calculations (PDF)

AUTHOR INFORMATION

Corresponding Authors

Liangliang Xu − *Department of Chemical and Biomolecular Engineering, Korea Advanced Institute of Science and Technology (KAIST), Daejeon 34141, Republic of Korea*; Email: xuliang@kaist.ac.kr

Il-Doo Kim − *Department of Materials Science and Engineering, Korea Advanced Institute of Science and Technology (KAIST), Daejeon 34141, Republic of Korea*; orcid.org/0000-0002-9970-2218; Email: idkim@kaist.ac.kr

Authors

Lu Song − *Department of Materials Science and Engineering, Korea Advanced Institute of Science and Technology (KAIST), Daejeon 34141, Republic of Korea*

Jaewan Ahn − *Department of Materials Science and Engineering, Korea Advanced Institute of Science and Technology (KAIST), Daejeon 34141, Republic of Korea*; orcid.org/0000-0002-0136-8427

Jong Won Baek − *Department of Materials Science and Engineering, Korea Advanced Institute of Science and Technology (KAIST), Daejeon 34141, Republic of Korea*

Euichul Shin − *Department of Materials Science and Engineering, Korea Advanced Institute of Science and Technology (KAIST), Daejeon 34141, Republic of Korea*

Complete contact information is available at: https://pubs.acs.org/10.1021/acssensors.2c01969

Notes

The authors declare no competing financial interest.

ACKNOWLEDGMENTS

This work was supported by the National Research Foundation of Korea (NRF) grant funded by the Korea government, Ministry of Science and ICT (grant no. 2020R1A2C301312711). This work was supported by Nano Convergence Foundation funded by the Ministry of Science and ICT (MSIT, Korea) & the Ministry of Trade, Industry and Energy (MOTIE, Korea) (no. 20000230). This work was also supported by Korea Electric Power Corporation (KEPCO) Research Institute (no. N06190047).

REFERENCES

(1) Wang, D.; Zhang, F.; Prabhakar, A.; Qin, X.; Forzani, E. S.; Tao, N. Colorimetric Sensor for Online Accurate Detection of Breath Acetone. *ACS Sens.* **2021**, *6*, 450−453.

(2) Zhou, C.; Meng, F.; Chen, K.; Yang, X.; Wang, T.; Sun, P.; Liu, F.; Yan, X.; Shimanoe, K.; Lu, G. High Sensitivity and Low Detection Limit of Acetone Sensor Based on NiO/Zn_2SnO_4 p-n Heterojunction Octahedrons. *Sens. Actuators, B* **2021**, *339*, 129912. February

(3) Wang, Z.; Hui, G.; Liu, J.; Yang, X.; Sun, C.; Liu, H.; Li, Z.; Zhu, M.; Pan, G. Highly Sensitive and Selective Sub Ppb Level Acetone Sensing Platform Based on Co_3O_4 −ZnO Heterojunction Composites. *Semicond. Sci. Technol.* **2021**, *36*, 095042.

(4) Zou, Y.; Chen, S.; Sun, J.; Liu, J.; Che, Y.; Liu, X.; Zhang, J.; Yang, D. Highly Efficient Gas Sensor Using a Hollow SnO_2 Microfiber for Triethylamine Detection. *ACS Sens.* **2017**, *2*, 897−902.

(5) Wang, D.; Huang, S.; Li, H.; Chen, A.; Wang, P.; Yang, J.; Wang, X.; Yang, J. Ultrathin WO_3 Nanosheets Modified by G-C_3N_4 for Highly Efficient Acetone Vapor Detection. *Sens. Actuators, B* **2019**, *2019*, 961−971.

(6) Roso, S.; Vilic, T.; Urakawa, A.; Llobet, E. Gas Sensing Properties of In_2O_3 Cubes Prepared by a Hydrothermal Method. *Proc. Eng.* **2016**, *168*, 247−250.

(7) Zahmouli, N.; Hjiri, M.; Leonardi, S. G.; El Mir, L.; Neri, G.; Iannazzo, D.; Espro, C.; Aida, M. S. High Performance Gd-Doped γ-Fe_2O_3 Based Acetone Sensor. *Mater. Sci. Semicond. Process.* **2020**, *116*, 105154.

(8) Hübner, M.; Simion, C. E.; Tomescu-Stănoiu, A.; Pokhrel, S.; Bârsan, N.; Weimar, U. Influence of Humidity on CO Sensing with P-Type CuO Thick Film Gas Sensors. *Sens. Actuators, B* **2011**, *153*, 347−353.

(9) Choi, P. G.; Fuchigami, T.; Kakimoto, K. I.; Masuda, Y. Effect of Crystal Defect on Gas Sensing Properties of Co_3O_4 Nanoparticles. *ACS Sens.* **2020**, *5*, 1665−1673.

(10) Majhi, S. M.; Naik, G. K.; Lee, H. J.; Song, H. G.; Lee, C. R.; Lee, I. H.; Yu, Y. T. Au@NiO Core-Shell Nanoparticles as a p-Type Gas Sensor: Novel Synthesis, Characterization, and Their Gas Sensing Properties with Sensing Mechanism. *Sens. Actuators, B* **2018**, *268*, 223−231.

(11) Li, D.; Tang, Y.; Ao, D.; Xiang, X.; Wang, S.; Zu, X. Ultra-Highly Sensitive and Selective H_2S Gas Sensor Based on CuO with

Sub-Ppb Detection Limit. *Int. J. Hydrogen Energy* **2019**, *44*, 3985−3992.
(12) Wang, T.; Li, Y.; Li, T.; Yu, H.; Yang, Y.; Yang, H.; Dong, X. Enhanced NOx Gas Sensing Properties of Cr_2O_3 Film Modified Ordered Porous ZnO Gas Sensors. *Solid State Ionics* **2018**, *326*, 173−182.
(13) Kortidis, I.; Swart, H. C.; Ray, S. S.; Motaung, D. E. Characteristics of Point Defects on the Room Temperature Ferromagnetic and Highly NO_2 Selectivity Gas Sensing of P-Type Mn_3O_4 Nanorods. *Sens. Actuators, B* **2019**, *285*, 92−107.
(14) Bettahar, M. M.; Costentin, G.; Savary, L.; Lavalley, J. C. On the Partial Oxidation of Propane and Propylene on Mixed Metal Oxide Catalysts. *Appl. Catal. A Gen.* **1996**, *145*, 1−48.
(15) Lou, X.; Han, J.; Chu, W.; Wang, X.; Cheng, Q. Synthesis and Photocatalytic Property of Co_3O_4 Nanorods. *Mater. Sci. Eng., B* **2007**, *137*, 268−271.
(16) Perekrestov, R.; Spesyvyi, A.; Maixner, J.; Mašek, K.; Leiko, O.; Khalakhan, I.; Maňák, J.; Kšírová, P.; Hubička, Z.; Čada, M. The Comparative Study of Electrical, Optical and Catalytic Properties of Co_3O_4 Thin Nanocrystalline Films Prepared by Reactive High-Power Impulse and Radio Frequency Magnetron Sputtering. *Thin Solid Films* **2019**, *686*, 137427.
(17) Li, Z.; Zhang, Y.; Zhang, H.; Yi, J. MOF-Derived Au-Loaded Co_3O_4 Porous Hollow Nanocages for Acetone Detection. *Sens. Actuators, B* **2021**, *344*, 130182.
(18) Li, K.; Li, X.; Chang, X.; Qiao, X.; Xiong, Y.; Xia, F.; Xue, Q. Metal-Organic Frameworks Derived Hierarchical Flower-like ZnO/Co_3O_4 Heterojunctions for Ppb-Level Acetone Detection. *Sens. Actuators, B* **2020**, *325*, 128814. May
(19) Su, M.; Zhou, W.; Liu, L.; Chen, M.; Jiang, Z.; Luo, X.; Yang, Y.; Yu, T.; Lei, W.; Yuan, C. Micro Eddy Current Facilitated by Screwed MoS2 Structure for Enhanced Hydrogen Evolution Reaction. *Adv. Funct. Mater.* **2022**, *32*, 2111067.
(20) Suh, J. M.; Sohn, W.; Shim, Y. S.; Choi, J. S.; Song, Y. G.; Kim, T. L.; Jeon, J. M.; Kwon, K. C.; Choi, K. S.; Kang, C. Y.; Byun, H. G.; Jang, H. W. P-p Heterojunction of Nickel Oxide-Decorated Cobalt Oxide Nanorods for Enhanced Sensitivity and Selectivity toward Volatile Organic Compounds. *ACS Appl. Mater. Interfaces* **2018**, *10*, 1050−1058.
(21) Jiang, Z.; Zhou, W.; Hong, A.; Guo, M.; Luo, X.; Yuan, C. MoS_2 Moiré Superlattice for Hydrogen Evolution Reaction. *ACS Energy Lett.* **2019**, 2830−2835.
(22) Zhou, W.; Chen, M.; Guo, M.; Hong, A.; Yu, T.; Luo, X.; Yuan, C.; Lei, W.; Wang, S. Magnetic Enhancement for Hydrogen Evolution Reaction on Ferromagnetic MoS_2 Catalyst. *Nano Lett.* **2020**, *20*, 2923−2930.
(23) Song, L.; Ahn, J.; Kim, D. H.; Shin, H.; Kim, I. D. Porous Pd-Sn Alloy Nanotube-Based Chemiresistor for Highly Stable and Sensitive H_2 Detection. *ACS Appl. Mater. Interfaces* **2022**, *14*, 28378−28388.
(24) Jiang, D. E.; Dai, S. The Role of Low-Coordinate Oxygen on Co_3O_4(110) in Catalytic CO Oxidation. *Phys. Chem. Chem. Phys.* **2011**, *13*, 978−984.
(25) Mortensen, J. J.; Hansen, L. B.; Jacobsen, K. W. Real-Space Grid Implementation of the Projector Augmented Wave Method. *Phys. Rev. B* **2005**, *71*, 1−11.
(26) Allouche, A. Software News and Updates Gabedit — A Graphical User Interface for Computational Chemistry Softwares. *J. Comput. Chem.* **2012**, *32*, 174−182.
(27) Park, H.; Oh, S.; Lee, S.; Choi, S.; Oh, M. Cobalt- and Nitrogen-Codoped Porous Carbon Catalyst Made from Core−Shell Type Hybrid Metal−Organic Framework (ZIF-L@ZIF-67) and Its Efficient Oxygen Reduction Reaction (ORR) Activity. *Appl. Catal. B* **2019**, *2019*, 322−329.
(28) Yang, Y.; Wang, S.; Jiang, C.; Lu, Q.; Tang, Z.; Wang, X. Controlled Synthesis of Hollow Co-Mo Mixed Oxide Nanostructures and Their Electrocatalytic and Lithium Storage Properties. *Chem. Mater.* **2016**, *28*, 2417−2423.
(29) Wang, C.; Cui, X.; Liu, J.; Zhou, X.; Cheng, X.; Sun, P.; Hu, X.; Li, X.; Zheng, J.; Lu, G. Design of Superior Ethanol Gas Sensor Based on Al-Doped NiO Nanorod-Flowers. *ACS Sens.* **2016**, *1*, 131−136.
(30) Steinhauer, S.; Chapelle, A.; Menini, P.; Sowwan, M. Local CuO Nanowire Growth on Microhotplates: In Situ Electrical Measurements and Gas Sensing Application. *ACS Sens.* **2016**, *1*, 503−507.
(31) Zhang, J.; Tang, P.; Liu, T.; Feng, Y.; Blackman, C.; Li, D. Facile Synthesis of Mesoporous Hierarchical Co_3O_4-TiO_2 p-n Heterojunctions with Greatly Enhanced Gas Sensing Performance. *J. Mater. Chem. A* **2017**, *5*, 10387−10397.
(32) Liu, J.; Dai, M.; Wang, T.; Sun, P.; Liang, X.; Lu, G.; Shimanoe, K.; Yamazoe, N. Enhanced Gas Sensing Properties of SnO_2 Hollow Spheres Decorated with CeO_2 Nanoparticles Heterostructure Composite Materials. *ACS Appl. Mater. Interfaces* **2016**, *8*, 6669−6677.
(33) Wang, C.; Yin, L.; Zhang, L.; Xiang, D.; Gao, R. Metal Oxide Gas Sensors: Sensitivity and Influencing Factors. *Sensors* **2010**, *10*, 2088−2106.
(34) Kim, R.; Jang, J. S.; Kim, D. H.; Kang, J. Y.; Cho, H. J.; Jeong, Y. J.; Kim, I. D. A General Synthesis of Crumpled Metal Oxide Nanosheets as Superior Chemiresistive Sensing Layers. *Adv. Funct. Mater.* **2019**, *29*, 1−10.
(35) Ivanov, O.; Maradudina, O.; Lyubushkin, R. Grain Size Effect on Electrical Resistivity of Bulk Nanograined Bi_2Te_3 Material. *Mater. Charact.* **2015**, *99*, 175−179.
(36) Koo, W. T.; Yu, S.; Choi, S. J.; Jang, J. S.; Cheong, J. Y.; Kim, I. D. Nanoscale PdO Catalyst Functionalized Co_3O_4 Hollow Nanocages Using MOF Templates for Selective Detection of Acetone Molecules in Exhaled Breath. *ACS Appl. Mater. Interfaces* **2017**, *9*, 8201−8210.
(37) Yoon, J. W.; Kim, J. S.; Kim, T. H.; Hong, Y. J.; Kang, Y. C.; Lee, J. H. A New Strategy for Humidity Independent Oxide Chemiresistors: Dynamic Self-Refreshing of In_2O_3 Sensing Surface Assisted by Layer-by-Layer Coated CeO_2 Nanoclusters. *Small* **2016**, *12*, 4229−4240.
(38) Kumar, M.; Agrawal, A. V.; Kumar, R.; Venkatesan, S.; Zakhidov, A.; Yang, G.; Bao, J.; Kumar, M. Photoactivated Mixed In-Plane and Edge-Enriched p-Type MoS_2 Flake-Based NO_2 Sensor Working at Room Temperature. *ACS Sens.* **2018**, *3*, 998−1004.
(39) Min, S. K.; Kim, H.; Noh, Y.; Choi, K. S.; Chang, S. P. Fabrication of Highly Sensitive and Selective Acetone Sensor Using (p)-Co_3O_4 Nanoparticle-Decorated (n)-ZnO Nanowires. *Thin Solid Films* **2020**, *714*, 138249.
(40) Liu, J.; Ke, J.; Li, Y.; Liu, B.; Wang, L.; Xiao, H.; Wang, S. Co3O4 Quantum Dots/TiO_2 Nanobelt Hybrids for Highly Efficient Photocatalytic Overall Water Splitting. *Appl. Catal. B* **2018**, *236*, 396−403. February
(41) Zhou, T.; Liu, X.; Zhang, R.; Wang, Y.; Zhang, T. NiO/$NiCo_2O_4$ Truncated Nanocages with PdO Catalyst Functionalization as Sensing Layers for Acetone Detection. *ACS Appl. Mater. Interfaces* **2018**, *10*, 37242−37250.
(42) Xiong, Z.; Hu, C.; Luo, X.; Zhou, W.; Jiang, Z.; Yang, Y.; Yu, T.; Lei, W.; Yuan, C. Field-Free Improvement of Oxygen Evolution Reaction in Magnetic Two-Dimensional Heterostructures. *Nano Lett.* **2021**, *21*, 10486−10493.
(43) Xu, Y.; Zheng, L.; Yang, C.; Liu, X.; Zhang, J. Highly Sensitive and Selective Electronic Sensor Based on Co Catalyzed SnO_2 Nanospheres for Acetone Detection. *Sens. Actuators, B* **2020**, *304*, 127237.
(44) Zhang, Y.; Jia, C.; Kong, Q.; Fan, N.; Chen, G.; Guan, H.; Dong, C. ZnO-Decorated In/Ga Oxide Nanotubes Derived from Bimetallic In/Ga MOFs for Fast Acetone Detection with High Sensitivity and Selectivity. *ACS Appl. Mater. Interfaces* **2020**, *12*, 26161−26169.
(45) Chang, X.; Qiao, X.; Li, K.; Wang, P.; Xiong, Y.; Li, X.; Xia, F.; Xue, Q. UV Assisted Ppb-Level Acetone Detection Based on Hollow ZnO/MoS_2 Nanosheets Core/Shell Heterostructures at Low Temperature. *Sens. Actuators, B* **2020**, *317*, 128208. February

https://doi.org/10.1021/acssensors.2c01969
ACS Sens. 2022, 7, 3540−3550

(46) Cho, H. J.; Choi, S. J.; Kim, N. H.; Kim, I. D. Porosity Controlled 3D SnO_2 Spheres via Electrostatic Spray: Selective Acetone Sensors. *Sens. Actuators, B* **2020**, *304*, 127350.
(47) Ma, A.; Baek, S. Y.; Seo, J. H.; Abbas, S. A.; Kwon, J. H.; Ahn, S. J.; Nam, K. M. Photodeposition of Pt Nanoparticles on Co_3O_4 nanocubes for Detection of Acetone at Part-per-Billion Levels. *ACS Appl. Nano Mater.* **2021**, 2572−2759.
(48) Jang, J. S.; Choi, S. J.; Kim, S. J.; Hakim, M.; Kim, I. D. Rational Design of Highly Porous SnO_2 Nanotubes Functionalized with Biomimetic Nanocatalysts for Direct Observation of Simulated Diabetes. *Adv. Funct. Mater.* **2016**, *26*, 4740−4748.
(49) Hu, J.; Yang, J.; Wang, W.; Xue, Y.; Sun, Y.; Li, P.; Lian, K.; Zhang, W.; Chen, L.; Shi, J.; Chen, Y. Synthesis and Gas Sensing Properties of NiO/SnO_2 Hierarchical Structures toward Ppb-Level Acetone Detection. *Mater. Res. Bull.* **2018**, *102*, 294−303. February
(50) Sui, N.; Wei, X.; Cao, S.; Zhang, P.; Zhou, T.; Zhang, T. Nanoscale Bimetallic AuPt-Functionalized Metal Oxide Chemiresistors: Ppb-Level and Selective Detection for Ozone and Acetone. *ACS Sens.* **2022**, *7*, 2178−2187.
(51) Zhang, S.; Yang, M.; Liang, K.; Turak, A.; Zhang, B.; Meng, D.; Wang, C.; Qu, F.; Cheng, W.; Yang, M. An Acetone Gas Sensor Based on Nanosized Pt-Loaded Fe_2O_3 Nanocubes. *Sens. Actuators, B* **2019**, *2019*, 59−67.
(52) Wongrat, E.; Chanlek, N.; Chueaiarrom, C.; Thupthimchun, W.; Samransuksamer, B.; Choopun, S. Acetone Gas Sensors Based on ZnO Nanostructures Decorated with Pt and Nb. *Ceram. Int.* **2017**, *43*, S557−S566. May

https://doi.org/10.1021/acssensors.2c01969
ACS Sens. 2022, 7, 3540−3550